npj | 2D materials and applications

Article

Published in partnership with FCT NOVA with the support of E-MRS

https://doi.org/10.1038/s41699-025-00601-0

Transient photodoping and phonon dynamics in bulk and monolayer MoS_2 by time resolved Raman scattering

A. M. Finardi[1,2], C. Fasolato[3,4] ✉, A. Giugni[1,2] ✉, M. Capeccia[4], R. Cucini[2], E. Cappelluti[5], F. Sacchetti[6], G. Panaccione[2], P. Postorino[4], C. Petrillo[6,7] & G. Rossi[1,2]

We study the phonon dynamics of bulk and monolayer MoS_2 under strong, transient photodoping by time resolved spontaneous Raman scattering (TRRS). By measuring the frequency and effective temperature evolution of each Raman active mode, TRRS allows to map the doping-induced changes in the phonon spectrum and to assess the energy transfer between the electron and phonon degrees of freedom. Our results demonstrate the occurrence of a photodoping-induced phonon renormalization and represent a first direct observation of a clear difference in the electron-phonon coupling between the "hot", strongly coupled A-symmetry mode and the "colder" E-symmetry one. We provide a model to map the energy redistribution in bulk and monolayer MoS_2, describing their different relaxation dynamics. We demonstrate that detailed information on the electronic behaviour can be drawn by probing the phonon dynamics by TRRS. That allows envisioning the tuning of electronic and transport properties of semiconducting layered materials through phononic approaches.

Quasi-two-dimensional layered materials offer a vast playground for fundamental science studies while paving the way for realising flexible and miniaturised (opto)electronic devices. In this framework, unravelling the relaxation pathways of photoexcited electrons is of great applicative interest. Exploring electron-phonon coupling mechanisms, focusing on the role of the specific vibrational modes and their symmetry[1], might offer a new perspective to understand the transport properties of these materials and to tailor them by means of phononic approaches, such as selectively populating or depleting specific phonon modes[2]. Pump-probe spectroscopies, employing ultrashort laser pulses to excite and manipulate matter and probe its evolution over time, are ideal tools to approach these investigations. A significant body of studies is available on semiconducting transition metal dichalcogenides, materials suitable for many potential applications, and in particular on the prototypical system MoS_2. So far, time-resolved experiments on MoS_2 have mainly focused on electron dynamics, demonstrating the photoinduced renormalization of exciton and bandgap energies. The crucial role of the coupling with the phonon subsystem in determining the hot carrier relaxation dynamics has emerged from transient absorption measurements[3,4]. However, only indirect information on the phonon dynamics could be obtained by studying the time-dependence of the exciton energy[5] or by exploiting coherence effects[6].

Time-resolved spontaneous Raman scattering (TRRS) provides direct access to the incoherent phonon relaxation, as well as electron-phonon coupling dynamics[7]. Indeed, TRRS enables direct insights into the transient Raman scattering cross section, which contains information on phonon frequency, symmetry (by polarization selection rules), lifetime (from the linewidth), and population (from the antiStokes/Stokes intensity ratio). Insights into electron-phonon coupling can also be retrieved from resonant Raman effects[8]. Unlike the stimulated Raman scattering technique, which probes the nonlinear response in a four-wave mixing scheme[9], spontaneous TRRS directly accesses the ground state phononic properties of a system under out-of-equilibrium condition.

Here we report on a comprehensive TRRS study on bulk and monolayer (1 L) MoS_2. Time evolution of two Raman-active phonons for bulk/1 L samples, namely the out-of-plane A_{1g}/A'_1 and in-plane E^1_{2g}/E' modes, is carefully monitored after the nearly resonant photoexcitation at the K point of the Brillouin Zone (BZ). We thus provide access to the electron-phonon interaction and to the relevant stages and timescales of hot carrier relaxation for both systems. Our results

[1]Dipartimento di Fisica, Università degli Studi di Milano, Milano, Italy. [2]CNR-Istituto Officina dei Materiali (IOM), Basovizza (TS), Italy. [3]CNR-Istituto dei Sistemi Complessi (ISC), Sapienza Università di Roma, Roma, Italy. [4]Dipartimento di Fisica, Sapienza Università di Roma, Roma, Italy. [5]CNR-Istituto di Struttura della Materia (ISM), Trieste, Italy. [6]Dipartimento di Fisica e Geologia, Università degli Studi di Perugia, Perugia, Italy. [7]AREA Science Park, Padriciano (TS), Italy.
✉e-mail: claudia.fasolato@uniroma1.it; andrea.giugni@unimi.it

demonstrate a phonon renormalization produced by the system transient doping and provide for the first time a direct observation of a different electron-phonon coupling between the *hot*, strongly coupled, A-symmetry mode and the more weakly coupled *colder* E-symmetry one. By *hot*, in this context, we refer to the population of a specific phonon mode, described by a statistical distribution with an equivalent temperature that exceeds that of other modes. Our measurements highlight the complexity of the electron coupling with the phonon subsystems as well as the capability of TRRS in mapping differences even between zone-center optical modes with only a few cm^{-1} energy separation. Overall, we draw detailed information on the electronic behaviour by probing phonons: these results suggest phonon dynamics as a powerful approach to tune and engineer electronic and transport properties.

Results

MoS_2 Raman spectra: continuous vs pulsed laser excitation

Figure 1a shows the structure of the investigated systems: bulk MoS_2, where no substrate effects are expected; 1 L MoS_2/ITO, i.e. single-layer MoS_2 on an indium tin oxide substrate, which is thermally insulating and electrically conductive; 1 L MoS_2/Au, i.e. single-layer MoS_2 on a gold substrate, which is both thermally and electrically conductive. In Fig. 1b, we show their Raman spectra collected under continuous wave (CW) compared to pulsed laser excitation. CW excitation was employed to precisely assess the equilibrium phonon frequency and bandwidth (see Fig. S0 in the Supplementary Information, SI). The Raman spectrum of MoS_2 in the considered frequency range comprises two main phonon modes: one is of symmetry E^1_{2g} in the bulk (measured at $\tilde{\nu} = 383\,cm^{-1}$) and E' in the 1 L (measured at $\tilde{\nu} = 384\,cm^{-1}$ on Au), herein indicated as E mode; one is of symmetry A_{1g} in the bulk ($\tilde{\nu} = 407\,cm^{-1}$) and A'_1 in the 1 L ($\tilde{\nu} = 404\,cm^{-1}$ on Au), herein termed A mode[10]. The spectrum includes a two-phonon feature at about $450\,cm^{-1}$, ascribed to the combined excitation of two longitudinal acoustic modes[11]. A redshift of about $1\,cm^{-1}$ is observed on ITO as compared to Au, and ascribed to substrate effects, i.e. strain or intrinsic doping[12–15]. From Fig. 1b, it is evident that the pulsed laser excitation leads to a significant broadening and overlap between the two main phonon spectral lines, especially in the 1 L samples, where the two modes occur at closer energies[10,12]. In a spontaneous TRRS experiment, the spectral resolution is indeed limited by the probe pulse bandwidth, which is in turn connected to the overall time resolution. The time-bandwidth product is set by the Fourier transform limit, so that the relation $\Delta t \Delta \tilde{\nu} \sim 15\,cm^{-1}ps$ connects the achieved spectral resolution $\Delta \tilde{\nu}$ given a pulse duration Δt. Thus, for appreciating a $15\,cm^{-1}$ phonon lineshape, the time resolution is limited to the *ps* scale.

In Fig. 1c, we present a sketch of the pump-probe TRRS experimental setup. The probe pulse is delivered to the sample after a spectral shaping through a 4f pulse shaper, setting the time-spectral resolution (see Methods for details). The nearly resonant pump ($633nm$, $\Delta t = 0.6ps$, shown in red) and probe ($513nm$, $\Delta t = 1ps$, shown in green) pulses are focused on the sample by a parabolic off-axis mirror; their relative delay is tuned in the -5 to 500 *ps* range through a delay line on the probe optical path (negative delays indicate the probe arrives on the sample *before* the pump, thus assessing the unperturbed sample state).

Time evolution of spectral shapes

TRRS spectra in the pump-probe delay interval -3–500 *ps* are presented in Fig. 2 and Fig. 3. The structure of Figs. 2 and 3 is the same, with data relative to bulk and 1 L MoS_2/ITO samples, respectively. In panels (a), data for both Stokes and antiStokes signals (simultaneously acquired) are shown as an intensity map. To highlight the pump-induced spectral modifications, in panels (c) we show the difference spectra, obtained by subtracting the response in absence of the pump to each pump-probe trace. Spectra and differences at selected delays are presented in panels (b) and (d).

In both bulk and 1 L MoS_2/ITO, the pump excitation induces a phonon mode softening along with a peak broadening within the first ps interval, as evident from Figs. 2a, b and 3a, b. While both frequencies and linewidths relax towards their pre-pump values at longer delay times, significant differences between the two systems emerge. Indeed, Figs. 2c, d and 3c, d show that the relaxation dynamics in the 1 L sample is completed within the probed delay window, since only a negligible difference signal is detectable after ~100 *ps*. By contrast, in the bulk sample, pump-induced effects persist over the whole 500 *ps* window with still clearly red-shifted peak positions.

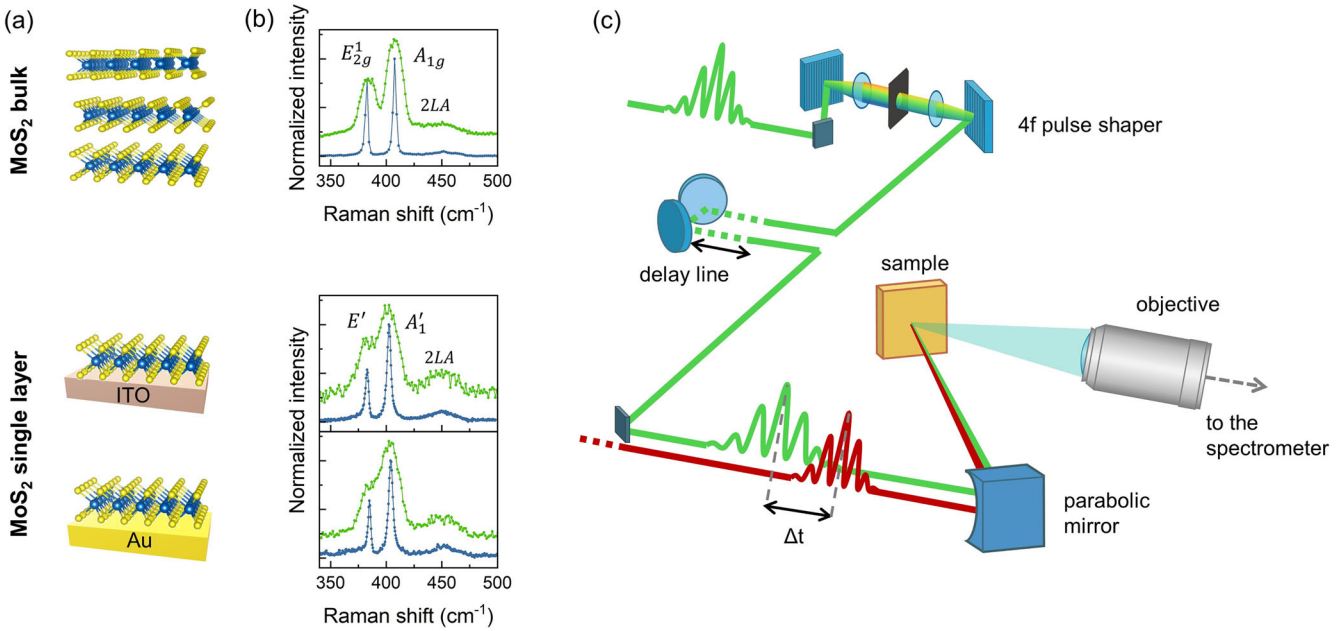

Fig. 1 | Experimental design. a Investigated samples (bulk MoS_2, 1 L MoS_2/ITO and 1 L MoS_2/Au) and **b** corresponding Stokes Raman spectra excited with a 532 nm CW (blue) and 513 nm, 1-ps pulsed (green) laser. **c** Schematics of the experimental setup for TRRS. The duration of both probe and pump laser pulses is set using a 4f pulse shaper (here sketched only for the probe beam). The pump-probe delay is set with a motorised delay line on the probe optical path. The beams are superimposed and focused by an off-axis parabolic mirror. The scattered radiation is collected with a long working distance 10x objective and analysed by a single-pass dispersive spectrometer.

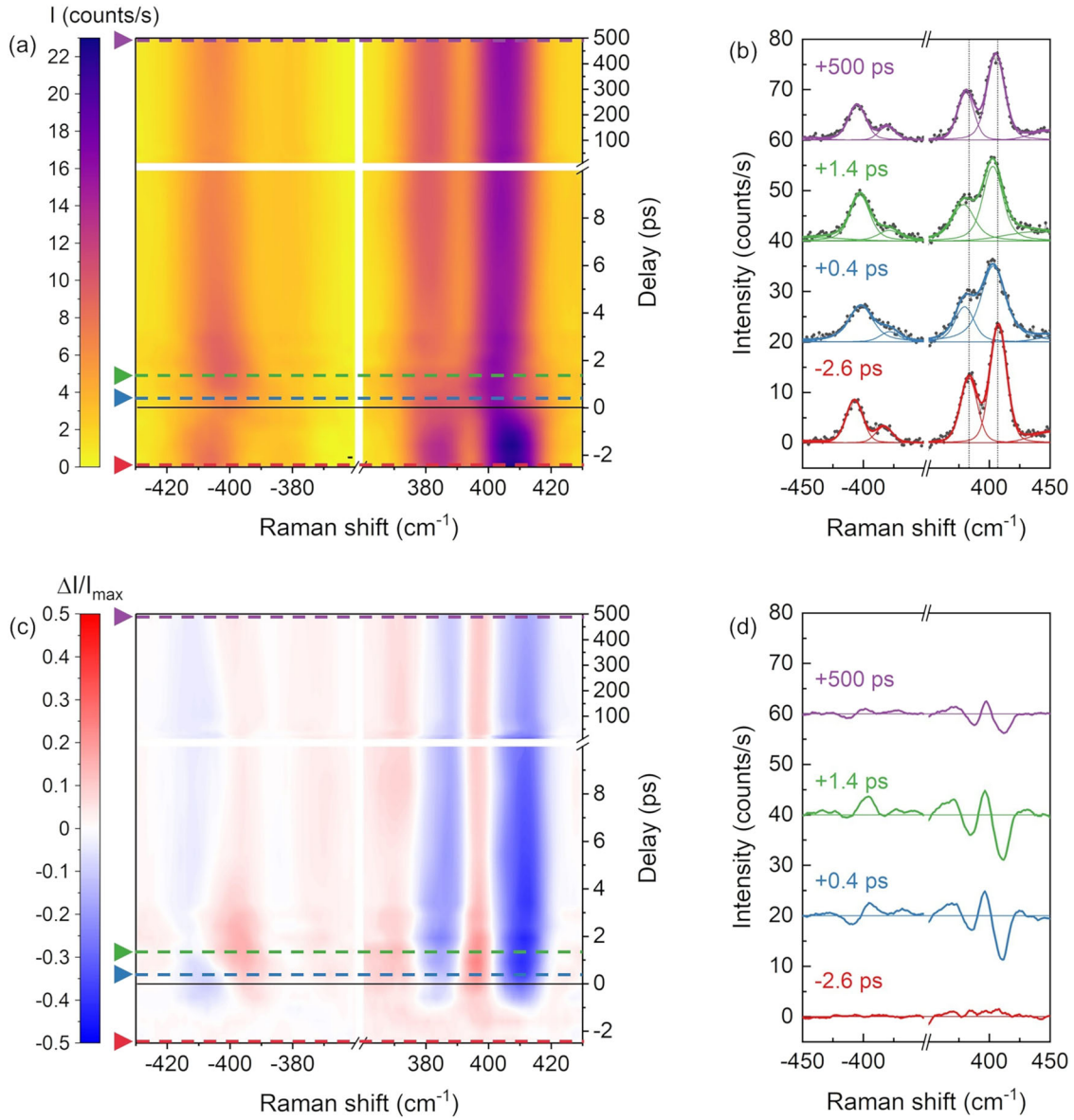

Fig. 2 | Time-resolved Raman scattering spectra and differences for bulk MoS_2. **a** Intensity map of the spectra (after a linear background subtraction and a 5-points smoothing) versus pump-probe delay. *A* and *E* phonons are clearly visible on both the Stokes (right) and antiStokes (left) sides. Dashed lines mark the selected spectra presented, with their multipeak fitting, in (**b**). **c** Intensity map of the relative difference between the spectra obtained with and without the pump (intensity differences are normalized to the maximum intensity in panel (**a**)). **d** Selected difference spectra (same delays as in (**b**)).

Looking at the Raman signal intensity, one notices that photoexcitation in the 1 L sample determines an overall enhancement of the signal, appearing as a positive trace (red area) in Fig. 3c; in the bulk, instead, the signal is reduced, as particularly evident on the Stokes side (blue area in Fig. 2c, accompanied by a red area arising due to peak frequency shift). We believe this observation is related to the partially resonant nature of Raman scattering in the present conditions, further commented in Section "Resonance Raman effects".

For both bulk and 1 L samples, the antiStokes-to-Stokes intensity ratios show qualitatively similar dynamical changes although developing over rather different timescales. The results obtained on the two 1 L samples are similar, as shown in Fig. S1 in the SI (data from 1 L MoS_2/Au).

The standard fitting of the spectra, with a multiple peak deconvolution, enables a quantitative analysis of the data, which is presented in the next section. The *A* and *E* phonon peaks were fitted with Lorentzian functions convolved with a Gaussian providing the appropriate spectral resolution, set from fitting the probe laser line. The two-phonon peak was fitted with a single, broad Gaussian function. The fit results on selected spectra are presented along with the data in Figs. 2b and 3b.

Pump-induced phonon renormalization and population evolution

In our setup, the *ps* probe pulse duration exceeds the timescale of electron-electron interaction[16]. This framework allows us to employ a multiple energy reservoir picture for the interpretation of TRRS data[7], where each reservoir (electrons, and specific phonon modes) obeys at each time delay an internal equilibrium statistics associated with a different effective temperature. This approach permits thus to monitor the redistribution of energy, initially deposited by the pump in the electron subsystem, among the various degrees of freedom, therefore probing the electron-phonon coupling dynamics. The timescale of the observed spectral changes can be exploited to trace back their microscopic origin, as discussed in the following. The simultaneous measurement of both the Stokes and antiStokes sides of the TRRS spectrum allows to extract the equivalent phononic temperature for each mode

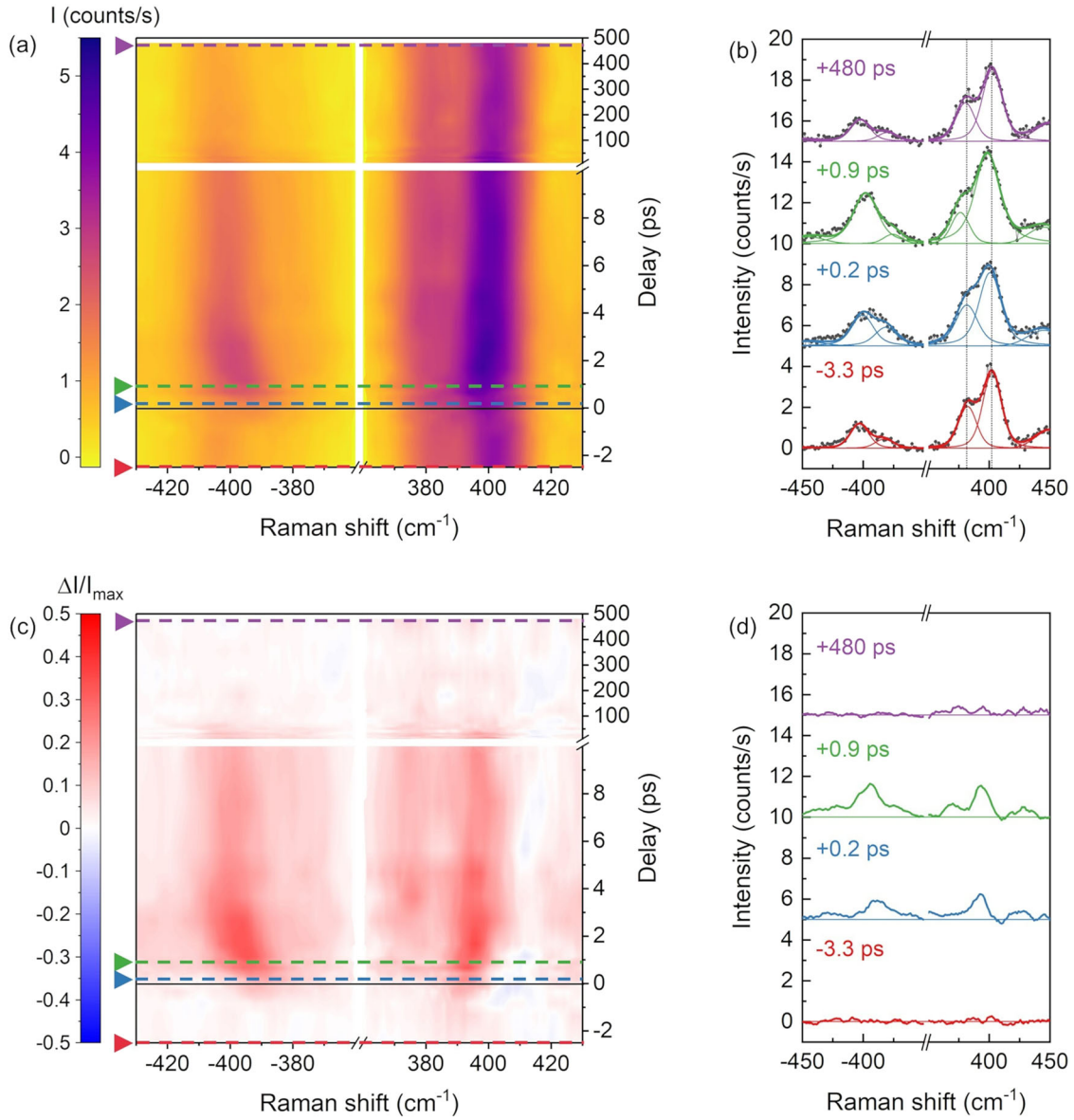

Fig. 3 | Time-resolved Raman scattering spectra and differences for 1 L MoS_2/ITO. a Intensity map of the spectra (after a linear background subtraction and a 5-points smoothing) versus pump-probe delay. *A* and *E* phonons are clearly visible on both the Stokes (right) and antiStokes (left) sides. Dashed lines mark the selected spectra presented, with their multipeak fitting, in (**b**). **c** Intensity map of the relative difference between the spectra obtained with and without the pump (intensity differences are normalized to the maximum intensity in (**a**)). **d** Selected difference spectra (same delays as in (**b**)).

via the well-known relation

$$\frac{I_{AS}}{I_S} = \left(\frac{\hbar\omega_l + \hbar\omega_v}{\hbar\omega_l - \hbar\omega_v}\right)^3 \frac{n_B}{n_B + 1} = \left(\frac{\hbar\omega_l + \hbar\omega_v}{\hbar\omega_l - \hbar\omega_v}\right)^3 e^{-\frac{\hbar\omega_v}{k_B T}} \quad (1)$$

where I_{AS} and I_S are the antiStokes and Stokes intensities (in the present case, the integrated intensity of the peaks, obtained from data fitting), $\hbar\omega_l$ and $\hbar\omega_v$ are the laser and phonon energies, and n_B is the Bose-Einstein distribution[8]. We remark that the T extracted from this equation can be considered as an effective "local" temperature in time, representative of the average phonon population at each pump-probe delay. Based on this definition, the terms *hot/cold* are used throughout the text to refer to the statistics describing the population of a specific excitation in the system. In Eq. (1), we neglected the possible effect of a wavelength dependence of the sample optical constants. In section S2 of the SI (including Fig. S6) we show that, even if this dependence could affect the temperature values extracted for the bulk sample, it would not have any effect on the measured dynamics.

In the following we focus, as main objects of our investigation, on the time dynamics of the frequencies $\tilde{\upsilon}_v$ and effective temperatures T_v for both the *A* and *E* lattice modes. To extract the characteristic time constants of the observed dynamics, the data were fitted with the function

$$f(t) = \alpha\theta(t - t_0)\left(e^{-\frac{t-t_0}{\tau_1}} + \delta e^{-\frac{t-t_0}{\tau_2}}\right) + k_{eq} \quad (2)$$

which was used for all the time dependent quantities throughout the paper. It is characterised by a step rise centred at t_0 and a biexponential decay with time constants τ_1 and τ_2, with $\tau_1 < \tau_2$. Here, α indicates the amplitude of the faster time trend (negative for the phonon frequencies), δ is the relative weight of the slower time trend. k_{eq} indicates the equilibrium value of the fitted quantity. Function (2) was convoluted with a Gaussian accounting for the temporal resolution (fixed at 1.2 *ps*, see Methods).

In Fig. 4, we show the evolution of the measured *A* mode frequencies $\tilde{\upsilon}_A(t)$ and effective temperatures $T_A(t)$ for all the three samples as a function

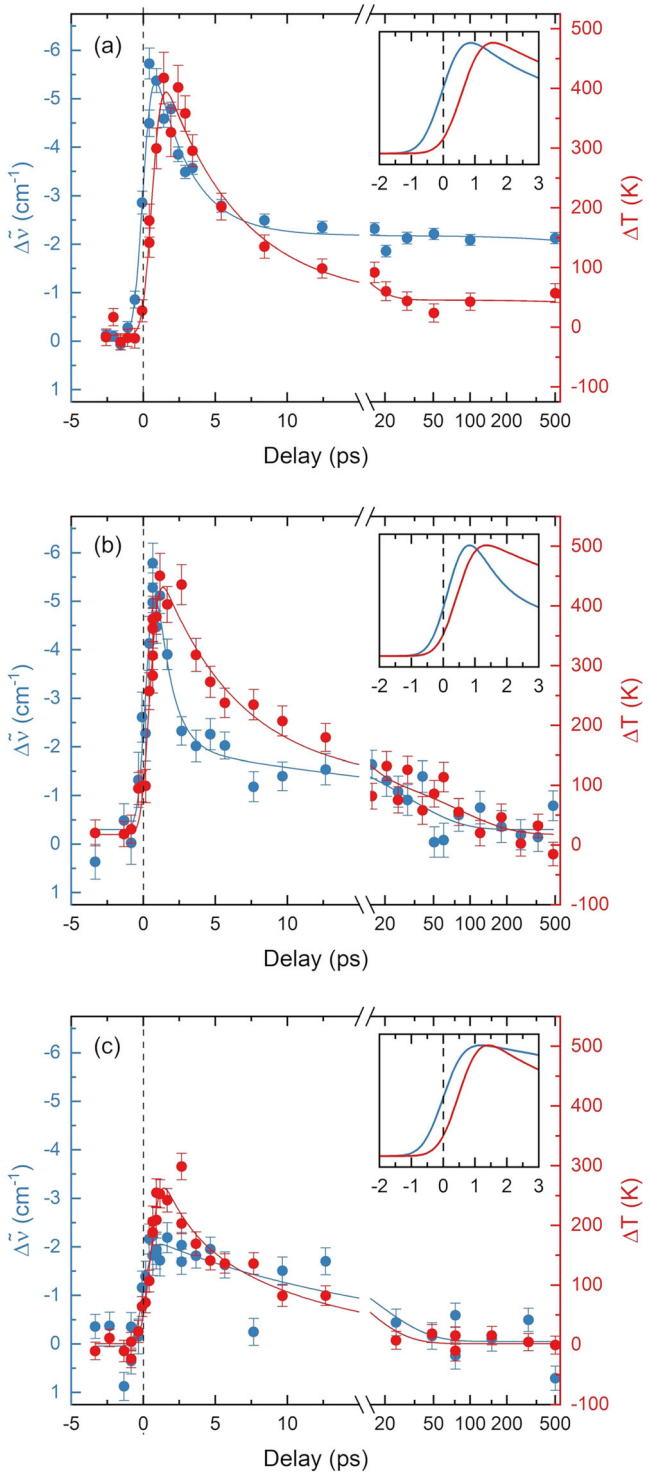

Fig. 4 | Comparison of the temporal evolution of the *A* mode frequency and equivalent phonon temperature in the three samples. The variation of the *A* phonon peak positions, from multipeak fitting, is displayed as blue dots, and the variation of the temperatures extracted from Eq. (1) as red dots for (**a**) bulk, (**b**) 1 L on ITO and (**c**) 1 L on Au samples. Continuous lines show the best fit curves. A dashed vertical line marks $t_0 = 0ps$. In the insets, we compare the fitting curves of frequency shift and temperature at short times, normalised to the maximum value, evidencing a clear delay between the rise of the two quantities.

of pump-probe delay. Solid lines are the best fit curve obtained from Eq. (2) with the time constants reported in Table 1. The behaviour qualitatively described in Section "Time evolution of spectral shapes" is clearly appreciated here: a prompt redshift of the phonon modes occurs right after the pump arrival, followed by a slow and sample-dependent relaxation dynamics. In all systems, we also observe a marked increase of the phononic temperature after photoexcitation: that reflects the expected rise in phonon population due the dissipation of the excess electron energy via electron-phonon coupling.

In Fig. 4a the bulk sample shows a nearly instantaneous drop ($t_0^{\tilde{\nu}_A} \sim 0ps$) of $\tilde{\nu}_A(t)$, reaching the maximum softening of $\Delta\tilde{\nu}_A^{\max} \sim -7\ cm^{-1}$ (extracted from the fit with function (2)). That is followed by a fast recovery dynamics ($\tau_1^{\tilde{\nu}_A} \sim 2ps$) and a consequent very slow one, exceeding the accessible delay window ($\tau_2^{\tilde{\nu}_A} \gg 500ps$). The phonon softening $\Delta\tilde{\nu}_A(t)$ is accompanied by an increase of the phonon temperature, $\Delta T_A(t)$, with $\Delta T_A^{\max} \sim 490K$. The subsequent relaxation dynamics is well reproduced with a fast decay time constant $\tau_1^{T_A} \sim 5ps$ and a longer one $\tau_2^{T_A} \gg 500ps$ as occurred for the frequency shift. Remarkably, the rise of $T_A(t)$ is delayed of $t_0^{T_A} \sim 0.6ps$ with respect to the phonon frequency shift. This observation occurs in all three samples (insets of Fig. 4) and plays a relevant role in rationalizing the origin of the phonon softening.

Although the softening of phonon frequencies can be due to lattice thermal expansion[8,17–21], in the present case phonon softening occurs before the increase of T_A, *i.e.* before the energy transfer from electron to phonon bath. That suggests the observed phonon redshift in the early time range to be primarily electronic in origin. Phonon frequency renormalization has been indeed observed in gated samples of MoS_2 and other TMDs[22–24], where it has been associated to the effect of the electron-phonon screening induced by carrier injection[24,25]. A similar, even stronger effect was predicted theoretically to occur following photodoping, leading to a large, expected phonon softening in ultrafast non-equilibrium measurements[26]. Girotto et al. estimated an expected frequency shift in the order of 10 cm^{-1} upon an initial excited carrier density of $10^{14}\ cm^{-2}$ for 1 L MoS_2. Such values are compatible with the present experimental conditions (see Methods): with the employed pump fluences, we expect a photoexcited carrier density of $10^{14}\ cm^{-2}$ in the 1 L samples and, equivalently, of $10^{21}\ cm^{-3}$ in the bulk[27,28]. We thus ascribe the prompt frequency shift in the early *ps* range to the enhanced screening induced by the resonant pump-driven transient doping of the system at the valleys. Moreover, we can expect the redistribution of both electron and hole excited carrier densities to be responsible for the short time relaxation dynamics. The fast decay can be most likely associated to non-radiative processes[16], rather than radiative recombination, typically occurring on a longer timescale[29–32].

Within this context, further insights can be retrieved from the comparison between the bulk system and 1 L samples on substrates. The behaviour observed for 1 L MoS_2/ITO appears rather similar to the bulk in the early ps range, showing actually the same frequency shift and phonon temperature ($\Delta\tilde{\nu}_A^{\max} \sim -8\ cm^{-1}$, $\Delta T_A^{\max} \sim 480K$) and a slightly smaller fast decay time after photoexcitation $\tau_1^{\tilde{\nu}_A} = 1.0ps$), possibly reflecting the higher electrical conductivity of ITO compared with MoS_2 itself. As to the slower delay constants τ_2, 1 L MoS_2/ITO shows a striking difference with the bulk sample, since both $\tilde{\nu}_A(t)$ and $T_A(t)$ undergo a complete relaxation in the order of tens of ps (see Table 1).

The time-dependent phonon response in 1 L MoS_2/Au appears further different, pointing out the relevant role of the substrate. Even in this case, similarly to the sample on ITO, the relaxation dynamics is fully completed within 500 ps, for both $\tilde{\nu}_A(t)$ and $T_A(t)$. However, the frequency shift here is much smaller than in the 1 L MoS_2/ITO case and, more importantly, the relaxation dynamics lacks the first, fast decay component. This is particularly evident from Fig. 5a, where the *A* mode frequency shifts, $\Delta\tilde{\nu}_A(t)$, of the two 1 L samples are compared. A strong influence of the substrate on 1 L systems is not unexpected[10,12,13,33]. The work function of Au is greater than that of MoS_2 implying that the band alignment of the MoS_2-Au interface favours electron transfer from MoS_2 to Au. Hence, the substrate provides a very efficient dissipation channel for the excited carriers on timescales of about 10–100 fs[34–36]. We argue that this quenches the doping-induced

Table 1 | Time constants extracted from the fitting of the temporal trends

	$\tilde{\upsilon}_A$			$\tilde{\upsilon}_E$			T_A			T_E			
	t_0	τ_1	τ_2	t_0	τ_1	τ_2	t_0	τ_1	τ_2	t_0	τ_r	τ_1	τ_2
Bulk	0	2.5	»500	0	2.0	»500	0.6	5.4	»500	0.6	5.5	3.5	»500
1 L on ITO	0.2	1.0	31	0.2	2.3	28	0.4	5.3	81	-	-	-	-
1 L on Au	0	-	17	0	-	40	0.5	2.0	10	-	-	-	-

Time delays are expressed in ps. The t_0 values are obtained as a shared fitting parameter for the two phonon modes, both for the frequencies and the temperatures.

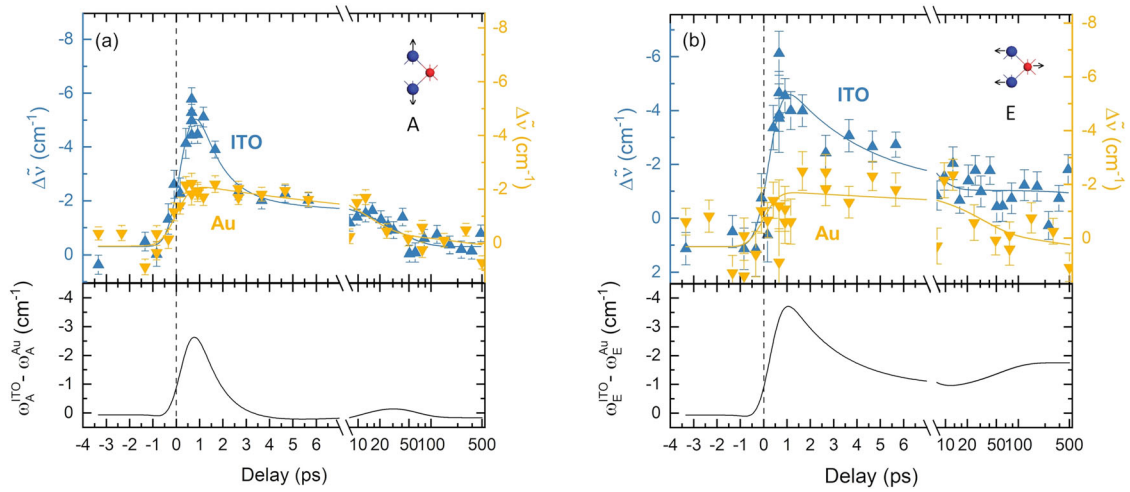

Fig. 5 | Effect of the substrate on the frequency shifts on 1L MoS_2. Data for ITO (blue) and Au (yellow), are shown for (**a**) *A* out-of-plane mode and (**b**) *E* in-plane mode. Continuous lines display the best fit curves. Bottom panels: differences between fitting curves on ITO and Au, rigidly shifted to a null difference at negative delays (thus, excluding pump-independent differences). At short delays, the difference is evident in both modes, whereas at long time delays a mismatch remains only for the *E* mode.

phonon renormalization faster than our temporal resolution. At longer time delays, as shown in Fig. 5a, the $\Delta\tilde{\upsilon}_A(t)$ trend for 1 L MoS_2/Au is basically superimposed to that of 1 L MoS_2/ITO, suggesting the slower relaxation dynamics being little affected by the substrate. This is quantitatively verified by the similar values of $\tau_2^{\upsilon_A}$ obtained by fitting on both samples.

Data and best fit curves on the time evolution of the *E* mode frequency renormalization $\Delta\tilde{\upsilon}_E$ are presented in Fig. S2 for the three samples. It is apparent that, in this strong photodoping regime, the renormalization of the *E* mode takes place to the same extent and with the same time dependence as that of the *A* mode. This observation results in comparable values of $\tilde{\tau_1^{\upsilon_v}}$ and $\tilde{\tau_2^{\upsilon_v}}$ estimated for each sample. Data in Fig. S2 also confirm the observations made above on the bulk, where the relaxation towards equilibrium is not completed in the studied time delay window, as well as the observation on the 1 L MoS_2/Au lacking the first, fast decay component.

The *E* mode frequency shifts for the two 1 L samples are also compared in Fig. 5b, evidencing a further difference between the two substrates. On Au, the *E* mode shift is basically the same as the *A* mode in terms of both amplitude and temporal dependence. In 1 L MoS_2/ITO, instead, the *E* mode shifts more than the *A* mode and does not return to equilibrium within 500*ps* (Fig. 5b). This asymptotic offset in the time decay of $\tilde{\upsilon}_E$ is estimated by fitting as $-1.9\,cm^{-1}$. We interpret the observation as due to strain. Indeed, lattice expansion of the substrate due to pump-induced heating can generate a tensile strain on 1 L MoS_2 which, acting along the in-plane directions, affects the *E* phonon frequency much more than the *A*[37–39]. This effect is more pronounced on ITO because of its thermal conductivity ($5W/mK$), much lower than that of gold ($317W/mK$) and of MoS_2 itself ($35W/mK$)[17,40]. Remarkably, only in the 1 L on ITO, the frequency shift appears delayed with respect to time zero (see insets of Fig. 4), as caused by the substrate-induced strain component in the observed shift.

Mode-dependent electron-phonon coupling

We now concentrate on the temperature dynamics of the *A* and *E* modes, as obtained from the antiStokes-to-Stokes intensity ratio. Out-of-equilibrium studies are often interpreted in the framework of two-temperature models, considering two different temperatures for the electronic and lattice subsystems in a transient configuration[41]. However, this picture has proven to be limiting in several materials[1,42,43]. That emerges clearly also from our data. The temperatures extracted from Eq. (1) for the *A* and *E* phonons in the three samples are shown in Fig. 6. The behaviour of the two modes appears dramatically different, regardless of the specific sample. The *A* mode temperatures are much higher than ambient temperature even at negative time delays and have a very prompt and marked increase of $\sim 300-400K$ after the pump arrival. On the other hand, the temperatures of the *E* mode are only slightly higher than room temperature ($\sim 290K$) at $t<0$, and display a slow and smooth increase of only $\sim 100-150K$ at positive delays.

The observation of a difference between the modes before time zero is remarkable per se. It is known from literature that electronic resonances can alter the antiStokes-to-Stokes intensity ratio, rendering Eq. (1) inapplicable. Some of these apparent temperature anomalies seem to arise from the different relative position of the antiStokes and Stokes transitions with respect to an electronic resonance, i.e. a peak of the joint density of states; that was also observed in $MoTe_2$[44]. Another possible reason for a failure of the simple picture of Eq. (1) might arise from symmetry-related differences in the resonant Raman cross sections for the two phonon modes[45]. In both these cases, the anomalies should be observed also in the equilibrium Raman spectra, acquired with the same probe wavelength. The spectral shape

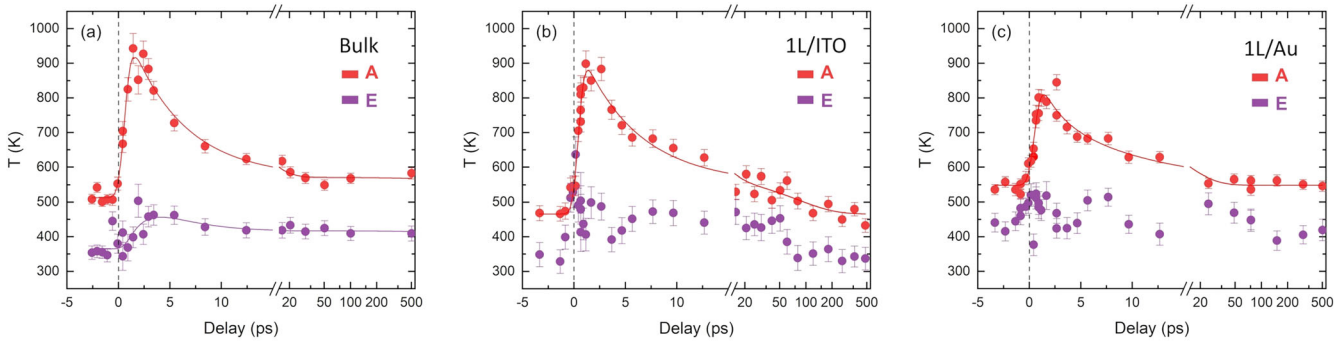

Fig. 6 | Phonon temperatures for the two phonon modes. Temperatures for bulk (**a**), 1 L on ITO (**b**), 1 L on Au (**c**) MoS_2 are estimated from the ratio between antiStokes and Stokes intensities from data fitting. Continuous lines display the results of the time trends fittings.

measured with a standard 532 nm CW probe (see Fig. S0 in the SI) is fully compatible with room temperature conditions and the extracted temperature appears on the contrary slightly enhanced (<40 K) for the E mode, as already observed in similar experimental conditions[46]. The difference in the mode temperatures appears only using a pulsed laser source, implying it is a non-equilibrium effect: we argue that the observation is a signature of a stronger coupling of the *A* phonons with the electronic degrees of freedom.

Given the probe wavelength is weakly resonant with the electronic transitions in MoS_2 (both bulk and 1 L), the relaxation of the small electron population excited by the probe itself creates an excess population of optical phonons within the probe duration. That is expected to contribute to the measured antiStokes intensity resulting in an increased effective *local* temperature in time. Electron-phonon coupling can thus be responsible for the imbalance in the initial ($t < 0$) population of *A* and *E* phonons. Since the enhancement of the base temperature of the *A* phonons is independent on the pump, this effect does not impair the interpretation of the pump-induced increase in phonon population and its relaxation dynamics, which are encoded in the observed variation ΔT with respect to the measurement without the pump (Fig. S4 in the SI).

The time evolution of $\Delta T(t)$ confirms that the *A* mode is more strongly coupled with the electron reservoir than the *E* mode, representing a prevalent electron-phonon scattering channel. Indeed, the increase in the *E* temperature is slower and we found that a smooth rise, modelled with an extra term $\left(1 - e^{-\frac{t-t_0}{\tau_r}}\right)$ in the fitting function (2), provides a better fit to the data than a step-like increase. The result of the fitting for the bulk, with $\tau_r \sim 5.5ps$, is shown on the data in Fig. 6a. The electron de-excitations via creation of *E* phonons result to occur at a lower rate than de-excitations involving *A* phonons. We remark that a second channel for *E* phonon creation is the anharmonic phonon-phonon relaxation. In the 1 L samples, the low intensity of the *E* antiStokes peak and the overlap with the *A* peak result in a lower accuracy of the fitted intensity and antiStokes-to-Stokes ratio. Thus, no fitting was performed on the T_E temporal trends, which in any case clearly follow, at short delays, the behaviour described for the bulk (see Fig. 6b, c).

By looking at the time trends of ΔT_A, ΔT_E (Fig. S4 in the SI), we can see how the population of the two modes becomes equal only at $t \gtrsim 20ps$ in all samples. This value can thus be taken as an estimate of the time after which a single temperature can adequately describe the entire phonon bath (or at least the optical phonons). It is evident that, at smaller delays, describing the phonon dynamics with less than two temperatures is not possible. Indeed, the *A* and *E* modes exhibit a "hot phonon" and a "cold phonon" behaviour, respectively, which necessarily derive from a very different symmetry-dependent coupling with the electrons[42,43]. Theoretical works reported in the literature have suggested that the out-of-plane atomic displacement, induced by the *A* phonons, modulates significantly the electronic band dispersion[47], and particularly the conduction band minima at the K point of the BZ. The in-plane distortion induced by *E* phonons is expected to have a minor effect on the electronic states[24].

System relaxation dynamics: overview

Based on the considerations above, we attempt to rationalize the consequent steps in the system relaxation dynamics, involving both electronic and phononic degrees of freedom.

We interpret the phonon renormalization at short delays as a signature of the transient, pump-driven photoexcited electron population. After ultrafast internal thermalization of the electrons to a pump-dependent temperature T_{el}, the carrier relaxation proceeds, determining the observed short time dynamics in the phonon frequencies. At the early ps scale, we can expect the carrier density to be depleted mainly via non-radiative processes (e.g. Auger, scattering by defects, charge transfer to the substrate in 1 L samples, etc.), whereas electron-phonon scattering provides a dissipation channel decreasing the effective electron temperature T_{el}. This goes along with an increase of the population of selected phonon modes, coupled to the photoinduced electron and hole charge pockets. In TRRS spectra, the dynamics of frequency shift and effective phonon temperature provide two independent useful channels for tracing these different physical processes, i.e. charge redistribution and energy transfer. In both, the influence of the substrate on the 1 L samples is evident. Concerning the carrier depletion (and associated frequency shift), we observe stronger deviations from the bulk behaviour for more efficient MoS_2-substrate charge transfer[34–36]. It is safe to assume that the transient phonon populations produced by electron relaxation do not contribute to any substantial modifications to the phonon spectrum at this timescale. Indeed, as expected from literature[48–50] and clearly observed in our measurements, at time delays shorter than 20*ps* the phonon distribution is highly non-thermal, with a marked difference in the population of different modes. Selectively populating some of the phonon modes does not inherently alter the equilibrium positions of the ions in the same way as thermodynamically increasing the temperature does, thus leaving the bond strength and phonon frequencies unperturbed.

As shown in the previous section, the electron-phonon driven increase in the effective lattice temperatures is highly mode-selective. We here introduce a multi-temperature model to describe the overall system relaxation dynamics. The model, developed following[42], is detailed in Section S4 of the SI. The result of its application to the bulk sample of this experiment is sketched in Fig. 7a. At the pump arrival, its energy is deposited in the electron subsystem, as visible from the increase in the electron temperature T_{el}. As the electron relaxation proceeds, with a *ps* delay with respect to the rise of T_{el}, the strongly coupled *A* phonon mode is first populated, then the equivalent temperature of the *E* mode grows, to reach a maximum at a few ps delay. The thermalization of the two modes with the phonon bath (i.e., all other phonon modes) occurs within 20*ps*. In the model, the electron-phonon coupling strengths and the modes specific heats are selected to closely follow the observed dynamics, in terms of kinetics and observed temperature variations. The experimental trends are properly reproduced by setting an electron-phonon coupling of the *A* phonon 10 times greater than the one of the *E* phonon. Overall, if an independent experimental

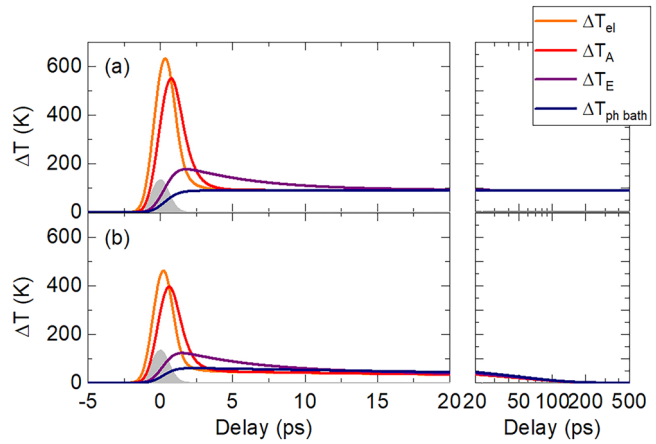

Fig. 7 | Multitemperature model describing the system relaxation dynamics. Sketch of the evolution of the internal temperature of the various subsystems interacting in the relaxation dynamics of: **a** bulk MoS_2; **b** 1 L MoS_2 on substrate. The pump temporal profile is displayed as the shadowed grey area. The time dependent temperature variations of the electrons, *A* and *E* symmetry phonons, and the phonon bath are displayed in solid lines with colours according to the legend (respectively, orange, red, purple, blue).

assessment of the photoexcited electron temperature were present, the model would allow a direct measurement, based on TRRS data, of the mode-dependent electron-phonon coupling strength.

At longer timescales, thermal and charge diffusion outside the scattering volume could be at work. In that case, the restoring of the initial charge/temperature conditions would be expected. Our findings suggest, however, that such diffusion processes are only weakly operative in the bulk system. Indeed, in the experiment conducted on the bulk, both the phonon frequencies and the phonon temperatures display a plateau behaviour for $t > 20ps$, with a residual frequency shift $\Delta\tilde{\nu}$ greater than 2 cm^{-1} and an excess of $55K$ in the phononic temperature of both modes at $t = 500ps$. Given this excess temperature does not explain the measured phonon shift[17–21] (see Fig. S5 in the SI), we conclude a finite transient doping is still present in the bulk compound at $t = 500ps$. That can be ascribed to long-lived excitons or trapped states[51]. Overall, the pump-driven excess energy is not fully dissipated, thus resulting in asymptotic temperatures exceeding the starting values for all the system degrees of freedom, as depicted in the right panel of Fig. 7a.

In both 1 L samples, the *short timescale* evolution of the phonon temperatures is similar to the bulk case. Here as well, at $t > 20ps$, lattice thermalization has occurred. The timescale is compatible with the (indirect) measurements of Chi et al.[5]. Interestingly, by calculating the phonon softening $\Delta\tilde{\nu}$ expected if the measured transient ΔT was reached under equilibrium conditions (Fig. S5 in the SI), one finds that for $t > 20ps$ the thermal contribution can fully explain the observed frequency shifts: contrary to what is observed in the bulk, electronic effects on the phonon spectrum in the 1 L appear negligible after a few tens of *ps*. This implies that the electronic relaxation processes in 1 L samples promptly damp the photodoping below the threshold needed to appreciate its effect on the phonon spectrum. Beside the possible charge transfer to the substrate, carrier de-excitation is indeed expected to be faster in 1 L samples, where the direct bandgap allows for radiative recombination, than in the bulk, where it is entirely phonon-mediated and thus less efficient. In addition, a crystal surface typically contains a higher concentration of defects than the bulk, leading to a possible increase in defect-mediated non-radiative recombination in 1 L samples[52]. The difference between the 1 L on ITO and Au resides is in the efficiency of electron population depletion and thermal dissipation by the substrate, both higher in Au: coherently, in the 1 L/Au sample, both the $\tau_1^{T_A}$ and $\tau_2^{T_A}$ result smaller as compared to the 1 L/ITO. Instead, one can expect a similar phonon de-excitation pathway in the 1 L/ITO and bulk samples, given they are both governed by the in-plane heat diffusion inside MoS_2 (ITO has a very poor thermal conductivity). The fact that the long timescale relaxation in the phonon population on ITO differs from that of bulk MoS_2 further corroborates our interpretation on the role of the residual transient doping in keeping the bulk sample out of equilibrium. The loss of the pump-driven photoinduced charge/energy due to all these combined effects in 1 L samples on substrates can be also considered in the multi-temperature model, as discussed in Section S4 of the SI. The qualitative theoretical behaviour is displayed in Fig. 7b, showing the complete relaxation of the 1 L system, in substantial agreement with the experimental scenario.

Resonance Raman effects

Lastly, we comment on the reduction of the Raman signal observed only in the bulk sample after photoexcitation. First, we recall that an increase in the phonon population leads to an enhancement of the Raman intensities. In Section S3 in the SI (Fig. S7), we show the expected rise in each peak intensity based on the assessed effective temperature, in both bulk and 1 L cases. While in the latter, the temperature dependence reasonably explains the measured intensity trend, this is clearly not the case in the bulk, where a significant intensity reduction is appreciated, with an overall non-monotonic behaviour versus time. We can conclude that the observed signal reduction in the bulk sample originates from the part of the Raman cross section related to electronic resonance, rather than from the phonon population factor.

A similar effect has indeed been observed in semiconductor samples measured by TRRS when the probe energy matches an electronic transition of the system, leading to a resonant enhancement of the Raman cross section. In pump-probe TRRS, depopulating (populating) the VB (CB) via photoexcitation can reduce the probability of Raman transitions from the ground electronic state and thus dynamically quench the resonance[7,53]. In our case, the 2.4 eV probe energy is greater than the MoS_2 band gap and can induce electronic transitions. Both in 1 L and in bulk, however, the probe energy does not match a peak in the joint density of states and is thus considered only weakly resonant with the system. Therefore, it is difficult to adopt the same straightforward interpretation as for resonant experiments conducted on Si and WS_2[7,53]. Further analysis and discussion are provided in Section S3 in the SI, motivating future fundamental investigation on this system.

Discussion

We have exploited spontaneous time-resolved Raman spectroscopy to study the de-excitation dynamics of bulk and 1 L MoS_2 after photodoping. The technique allowed us to track both the changes of the phonon frequencies and the creation of an out-of-equilibrium phonon population, highlighting the different timescales of the two phenomena. We directly observed for the first time a transient renormalization of the phonon energies, expected by theoretical works in literature[26] as a consequence of doping-induced changes in the electron-phonon coupling. While the renormalization of a particular phonon is expected to originate from activation of the corresponding electron-phonon scattering channel, we observe here the softening to be faster than phonon population creation. We identified the main difference between the bulk and 1 L samples in the relaxation dynamics at long delays. The complete return to equilibrium is indeed observed only in the 1 L, as a consequence of the rapid relaxation of the excited carriers, allowed by the system 2D nature and direct bandgap. On the other hand, in the bulk, long-lived excited carriers continue to affect the phonon spectrum up to at least $500ps$.

Following the time evolution of two phonon modes of different symmetry, we discarded a description of the whole phonon bath with a single temperature at ultrashort delays from the optical pump. We observed in fact a much faster and larger increase in the temperature of the *A* phonons compared to the *E* phonons, and showed that reproducing the observed phenomenology with a multi-temperature model requires the use of at least 3 different temperatures for the phonon subsystem. This non-thermal

phonon distribution survives at least up to 20*ps*. A timescale of tens of *ps* for the thermalization of the phonon subsystem is consistent with the findings of Caruso[49] and Britt et. al.[48] which, however, describe the inhomogeneous excitation of the phonons across the BZ without appreciating a substantial difference between the *A* and *E* modes at Γ. Remarkably, the stronger coupling of the *A* phonons with the electrons cannot be inferred by the frequency renormalization, which involves both modes: apart from small strain effects on the 1 L/ITO, we showed that the *A* and *E* mode frequencies undergo the same softening and relaxation dynamics. The results of our out-of-equilibrium experiment therefore differ from the measurements performed on an electrostatically doped sample under equilibrium conditions reported in literature, showing a much greater redshift for the *A* phonon than for the *E* phonon. Our results are at odds as well with theoretical computations, predicting a stronger effect of transient photodoping on the *A* phonon frequencies[26].

In summary, our experiment provided direct access to the temporal evolution of phonon lineshapes and populations in MoS_2 upon the impulsive photoexcitation of a hot carrier population at the K point of the BZ. Our analysis shows how TRRS can provide a complete picture of the dynamical response of the system, as it enables to simultaneously map the response of the different phonon modes, while also indirectly accessing the electronic degrees of freedom. Overall, the results unravel the electron-phonon and phonon-phonon relaxation pathways, assessing the effect of dimensionality and, in the case of 1 L MoS_2, of the interaction with the substrate, on the electronic and thermal properties of a benchmark semiconducting TMD system. Further investigation will open the possibility to manipulate the photoexcited carrier relaxation pathways by tailored phonon excitation[2].

Methods

Samples

MoS_2 crystals were purchased from 2D Semiconductors Inc. (Scottsdale, AZ). Epitaxially grown, 1 L MoS_2 transferred on flat gold and ITO substrates was measured without further pretreatment. The bulk MoS_2 sample was obtained by exfoliating a $\sim 10\,\mu m$ crystal onto a diamond window. Diamond was selected as substrate because of flatness and because of the high thermal conductivity, minimizing sample damaging and enabling repeated measurements on the same spot.

Time resolved Raman spectroscopy

The experiment was performed in the pump-probe scheme depicted in Fig. 1c. Probe pulses with $\lambda = 513$ nm are obtained after a second harmonic generation process in a BBO crystal from the fundamental emission at 1026 nm of a Yb:KGW-based laser (PHAROS, Light Conversion) in 300 fs pulses, working at 50 kHz. The same laser seeds an optical parametric amplifier (OPA) generating $\lambda = 633$ nm (~ 1.96 eV) pump pulses, in resonance with the excitonic bandgap at the K point of the BZ. The time-spectral resolutions, 1 ps – 15 cm^{-1} and 0.6 ps – 45 cm^{-1} for the probe and pump, respectively, are set with two 4f pulse shapers. As the pump pulse generated from the OPA has a slight chirp, its duration was measured with a commercial autocorrelator (APE pulseCheck). The overall temporal resolution of ~1.2 ps was obtained from the cross-correlation of the pump and probe pulses, approximated with Gaussian profiles. A delay line on the probe optical path enables the tuning of the pump-probe relative delay. The two pulses are superimposed and focalized on the sample surface by a 45° off-axis parabolic mirror, resulting in a 25 μm spot diameter on sample. The best conditions for pump-probe spatial and temporal overlap were determined by monitoring the sum frequency generation from a suitably oriented BBO nonlinear crystal. The Raman scattering signal is collected at ~45° from the incident pulse direction by a 10x, long working distance objective, then delivering the signal to a single pass, dispersive spectrometer (Triax320, Horiba Scientific) equipped with multiple diffraction gratings and a liquid-cooled CCD. A holographic 1800 grooves/mm grating is used for the experiment, granting a spectral resolution of 3 cm^{-1}. Two notch filters remove the elastically scattered light at both the pump and probe wavelengths. The laser fluences employed in the experiment were: 15 mJ/cm^2 and 2.4 mJ/cm^2 for the pump and probe, respectively on the bulk sample, 5 mJ/cm^2 and 1.5 mJ/cm^2 on the 1 L/ITO sample, 2.5 mJ/cm^2 and 1.0 mJ/cm^2 on the 1 L/Au sample. It should be noted that in the last case, due to the high reflectivity of the Au substrate at the pump wavelength, the effective fluence on the 1 L sample is given by almost twice the impinging fluence, leading to a similar value for the pump to the one employed for the 1 L/ITO. The estimated charge densities produced by optical pumping are calculated based on the optical properties (reflectivity, absorption coefficient) of MoS_2 and, in the case of the 1 L samples, of the substrates[27,28]. That leads to excited carrier densities of 10^{14} cm^{-2} in the 1 L samples and 10^{21} cm^{-3} in the bulk (considering a uniform excitation over the pump penetration depth). We note that the latter value corresponds to an areal density of carriers of 10^{14} cm^{-2} for each layer. The employed pump powers lead all the systems to a high photodoping regime, while remaining below the sample damaging thresholds.

Data pretreatment and analysis

The multiple peak deconvolution was performed on the spectra according to the following procedure: the background was fitted with two different lines for the Stokes and antiStokes sides and subtracted; the probe laser line was acquired and fitted with a Gaussian function, obtaining the measurement spectral resolution; the *A* and *E* phonon peaks were fitted with Voigt functions (i.e. the convolution of a Lorentzian and a Gaussian) with the Gaussian FWHM fixed at the spectral resolution, while the broad peak at 450 cm^{-1} was fitted with a single broad Gaussian function. For each peak, Stokes and antiStokes sides were fitted simultaneously, with the same parameters describing the distance from the laser line and the FWHM. Having measured an additional spectrum without the pump after each pump-probe measurement, we were able to partially correct the possible effect of laser intensity fluctuations in the parameters extracted from the multipeak fitting. The values of the frequency shifts and the phonon temperature extracted from the unpumped spectra were subtracted to the corresponding quantities derived from the pump-probe spectra. The values presented in Fig. 6 were then obtained by summing back the average value of all unpumped spectra. The spectra acquired without the pump allowed also to verify the absence of degradation in the samples. A further fine correction of the zero-delay time measured with the BBO crystal was performed by adjusting to zero the fastest dynamics observed in the TR Raman temporal scan, which coincides with the frequency shift in MoS_2 bulk and in the 1 L MoS_2 on Au.

Data availability

Experimental data are available in txt form from the Zenodo database, https://doi.org/10.5281/zenodo.15807306.

Received: 15 April 2025; Accepted: 13 August 2025;
Published online: 02 September 2025

References

1. Sadasivam, S., Chan, M. K. Y. & Darancet, P. Theory of thermal relaxation of electrons in semiconductors. *Phys. Rev. Lett.* **119**, 136602 (2017).
2. Kumar, G. & Chung, P. W. Selective phonon stimulation mechanism to tune thermal transport. *ACS omega* **7**, 12787–12794 (2022).
3. Chi, Z., Chen, H., Zhao, Q. & Weng, Y. Observation of the hot-phonon effect in monolayer MoS_2. *Nanotechnology* **31**, 235712 (2020).
4. Wang, T. et al. Hot carrier cooling and trapping in atomically thin WS_2 probed by three-pulse femtosecond spectroscopy. *ACS Nano* **17**, 6330–6340 (2023).
5. Chi, Z. et al. Ultrafast energy dissipation via coupling with internal and external phonons in two-dimensional MoS_2. *ACS Nano* **12**, 8961–8969 (2018).

6. Sun, L. et al. Phonon Dephasing Dynamics in MoS2. *Nano Lett.* **21**, 1434–1439 (2021).
7. Shuangping, H. et al. Incoherent phonon population and exciton-exciton annihilation dynamics in monolayer WS_2 revealed by time-resolved resonance Raman scattering. *Opt. Express* **27**, 29949–29961 (2019).
8. Loudon, R. The Raman effect in crystals. *Adv. Phys.* **13**, 423–482 (1964).
9. Batignani, G., Ferrante, C., Fumero, G., Martinati, M. & Scopigno, T. Femtosecond stimulated Raman spectroscopy. *Nat. Rev. Methods Prim.* **4**, 34 (2024).
10. Zhang, X. et al. Phonon and Raman scattering of two-dimensional transition metal dichalcogenides from monolayer, multilayer to bulk material. *Chem. Soc. Rev.* **44**, 2757–2785 (2015).
11. Carvalho, B. R. et al. Intervalley scattering by acoustic phonons in two-dimensional MoS_2 revealed by double-resonance Raman spectroscopy. *Nat. Commun.* **8**, 1–8 (2017).
12. Capeccia, M., D'Alò, B. & Stellino, E. Investigating the effects of sample-substrate interaction in the Raman and photoluminescence spectrum of 1L-WS_2. *Il Nuovo Cim.* **100**, 47 (2024).
13. Buscema, M., Steele, G. A., van der Zant, H. S. J. & Castellanos-Gomez, A. The effect of the substrate on the Raman and photoluminescence emission of single-layer MoS_2. *Nano Res* **7**, 561–571 (2014).
14. Panasci, S. E. et al. Strain, doping, and electronic transport of large area monolayer MoS_2 exfoliated on gold and transferred to an insulating substrate. *ACS Appl. Mater. Interfaces* **13**, 31248–31259 (2021).
15. Stellino, E., D'Alò, B., Blundo, E., Postorino, P. & Polimeni, A. Fine-tuning of the excitonic response in monolayer WS_2 Domes via Coupled Pressure and Strain Variation. *Nano Lett.* **24**, 3945–3951 (2024).
16. Fasolato, C., Stellino, E., Sacchetti, F. & Petrillo, C. Fast plasma production by intense femtosecond extreme ultraviolet and x-ray pulses. *Phys. Rev. Res.* **7**, 013072 (2025).
17. Yan, R. et al. Thermal conductivity of monolayer molybdenum disulfide obtained from temperature-dependent Raman spectroscopy. *ACS Nano* **8**, 986–993 (2014).
18. Lanzillo, N. A. et al. Temperature-dependent phonon shifts in monolayer MoS_2. *Appl. Phys. Lett.* **103**, 093102 (2013).
19. Li, X. et al. Pressure and temperature-dependent Raman spectra of MoS_2 film. *Appl. Phys. Lett.* **109**, 242101 (2016).
20. Zhu, S. & Zheng, W. Temperature-dependent phonon shifts in van der Waals crystals. *J. Phys. Chem. Lett.* **12**, 5261–5270 (2021).
21. Lin, Z. et al. Thermal expansion coefficient of few-layer MoS_2 studied by temperature-dependent Raman spectroscopy. *Sci. Rep.* **11**, 7037 (2021).
22. Chakraborty, B. et al. Symmetry-dependent phonon renormalization in monolayer MoS_2 transistor. *Phys. Rev. B* **85**, 161403 (2012).
23. Lu, X. et al. Gate-Tunable resonant Raman spectroscopy of bilayer MoS_2. *Small* **13**, 1701039 (2017).
24. Sohier, T. et al. Enhanced electron-phonon interaction in multivalley materials. *Phys. Rev. X* **9**, 031019 (2019).
25. Novko, D. Broken adiabaticity induced by Lifshitz transition in MoS_2 and WS_2 single layers. *Commun. Phys.* **3**, 30 (2020).
26. Girotto, N., Caruso, F. & Novko, D. Ultrafast nonadiabatic phonon renormalization in photoexcited single-layer MoS_2. *J. Phys. Chem. C.* **127**, 16515–16524 (2023).
27. Ermolaev, G. A. et al. Broadband optical properties of monolayer and bulk MoS_2. *npj 2D Mater. Appl* **4**, 21 (2020).
28. König, T. A. F. et al. Electrically tunable plasmonic behavior of nanocube–polymer nanomaterials induced by a redox-active electrochromic polymer. *ACS Nano* **8**, 6182–6192 (2014).
29. Amani, M. et al. Near-unity photoluminescence quantum yield in MoS_2. *Science* **350**, 1065–1068 (2015).
30. Wang, H., Zhang, C. & Rana, F. Ultrafast Dynamics of Defect-Assisted Electron–Hole Recombination in Monolayer MoS_2. *Nano Lett.* **15**, 339–345 (2015).
31. Yu, Y. et al. Fundamental limits of exciton-exciton annihilation for light emission in transition metal dichalcogenide monolayers. *Phys. Rev. B* **93**, 201111 (2016).
32. Robert, C. et al. Exciton radiative lifetime in transition metal dichalcogenide monolayers. *Phys. Rev. B* **93**, 205423 (2016).
33. Sun, Y., Wang, R. & Liu, K. Substrate induced changes in atomically thin 2-dimensional semiconductors: Fundamentals, engineering, and applications. *Appl. Phys. Rev.* **4**, 011301 (2017).
34. Bhanu, U., Islam, M., Tetard, L. & Khondaker, S. I. Photoluminescence quenching in gold - MoS_2 hybrid nanoflakes. *Sci. Rep.* **4**, 5575 (2014).
35. Zhang, L. et al. Modulated interlayer charge transfer dynamics in a monolayer TMD/metal junction. *Nanoscale* **11**, 418–425 (2019).
36. Pincelli, T. et al. Observation of multi-directional energy transfer in a hybrid plasmonic–excitonic nanostructure. *Adv. Mater.* **35**, 2209100 (2023).
37. Kukucska, G. & Koltai, J. Theoretical investigation of strain and doping on the Raman spectra of monolayer MoS_2. *Phys. Status Solidi B* **254**, 1700184 (2017).
38. Zhu, C. R. et al. Strain tuning of optical emission energy and polarization in monolayer and bilayer MoS_2. *Phys. Rev. B* **88**, 121301(R) (2013).
39. Wang, Y., Cong, C., Qiu, C. & Yu, T. Raman spectroscopy study of lattice vibration and crystallographic orientation of monolayer MoS_2 under uniaxial strain. *Small* **9**, 2857–2861 (2013).
40. Kaźmierczak-Bałata, A., Bodzenta, J., Dehbashi, M., Mayandi, J. & Venkatachalapathy, V. Influence of post processing on thermal conductivity of ITO thin films. *Materials* **16**, 362 (2023).
41. Scotognella, F. et al. Plasmon dynamics in colloidal $Cu_{2-x}Se$ nanocrystals. *Nano Lett.* **11**, 4711–4717 (2011).
42. Cappelluti, E., Caruso, F. & Novko, D. Properties and challenges of hot-phonon physics in metals: MgB_2 and other compounds. *Prog. Surf. Sci.* **97**, 100664 (2022).
43. Mansart, B. et al. Temperature-dependent electron-phonon coupling in $La_{2-x}Sr_xCuO_4$ probed by femtosecond X-ray diffraction. *Phys. Rev. B* **88**, 054507 (2013).
44. Goldstein, T. et al. Raman scattering and anomalous Stokes–anti-Stokes ratio in $MoTe_2$ atomic layers. *Sci. Rep.* **6**, 28024 (2016).
45. Zardo, I. et al. E_1(A) electronic band gap in wurtzite InAs nanowires studied by resonant Raman scattering. *Nano Lett.* **13**, 3011–3016 (2013).
46. Sokalski, P. et al. Effects of hot phonons and thermal stress in micro-Raman spectra of molybdenum disulfide. *Appl. Phys. Lett.* **121**, 182202 (2022).
47. Ortenzi, L., Pietronero, L. & Cappelluti, E. Zero-point motion and direct-indirect band-gap crossover in layered transition-metal dichalcogenides. *Phys. Rev. B* **98**, 195313 (2018).
48. Britt, T. L. et al. Direct view of phonon dynamics in atomically thin MoS_2. *Nano Lett.* **22**, 4718–4724 (2022).
49. Caruso, F. Nonequilibrium lattice dynamics in monolayer MoS_2. *J. Phys. Chem. Lett.* **12**, 1734–1740 (2021).
50. Han, Z., Sokalski, P., Shi, L. & Ruan, X. Prediction of hot zone-center optical phonons in laser-irradiated molybdenum disulfide with a semiconductor multitemperature model. *Phys. Rev. B* **107**, L041407 (2023).
51. Goodman, A. J., Willard, A. P. & Tisdale, W. A. Exciton trapping is responsible for the long apparent lifetime in acid-treated MoS_2. *Phys. Rev. B* **96**, 121404 (2017).
52. Wang, H., Zhang, C. & Rana, F. Surface recombination limited lifetimes of photoexcited carriers in few-layer transition metal dichalcogenide MoS_2. *Nano Lett.* **15**, 8204–8210 (2015).
53. Zhu, J., Versteeg, R. B., Padmanabhan, P. & van Loosdrecht, P. H. M. Dynamical resonance quench and Fano interference in spontaneous Raman scattering from quasiparticle and collective excitations. *Phys. Rev. B* **99**, 094305 (2019).

Acknowledgements
G.P. and P.P. acknowledge support from Progetto PRIN 2022 "BEST-WIN" PNRR Next Generation EU—CUP B53D23004530006. E.C. acknowledges support from MUR, PRIN Project 2022WS9MS4. R.C. acknowledges the Italian Ministry of Foreign Affairs and International Cooperation (MAECI), Grant no. PGR12320—U-DYNAMEC—CUP B53C23006060001. M.C., E.C. and G.P. acknowledge financial support from PNRR MUR project PE0000023-NQSTI. C.P. acknowledges the agreement (*Accordo Quadro*) CarESS between Elettra Sincrotrone Trieste, INFN and the University of Perugia. This work was performed in the framework of the NFFA-SPRINT facility, supported by MUR as the Activity of International Relevance NFFA (www.trieste.nffa.eu).

Author contributions
C.F. and A.G. conceived the experiment and supervised the activities. A.M.F., C.F., A.G. and M.C. performed the measurements. A.M.F. and C.F. analysed experimental data and wrote the manuscript with support from A.G., M.C., R.C., E.C., P.P. and G.R. A.M.F., C.F., A.G., R.C., F.S., G.P., P.P., C.P. and G.R. were involved in the experimental apparatus design and development. E.C. developed the theoretical model. All authors discussed the results and reviewed the manuscript.

Competing interests
The authors declare no competing interests.

Additional information
Supplementary information The online version contains supplementary material available at https://doi.org/10.1038/s41699-025-00601-0.

Correspondence and requests for materials should be addressed to C. Fasolato or A. Giugni.